IEEE Access
Multidisciplinary : Rapid Review : Open Access Journal

Received 30 June 2026, accepted 6 August 2026, date of publication 14 August 2026, date of current version 20 August 2026.

Digital Object Identifier 10.1109/ACCESS.2026.3724004

RESEARCH ARTICLE

Design of a High-Power Filter Inductor for Variable-Switching-Frequency TCM-Based ZVS Inverters in EV Drive Systems

KHIZRA ABBAS[1], (Member, IEEE), BHASKAR CHATTERJEE[2], (Student Member, IEEE), ANTONIO CAMEO DEL REY[1], (Student Member, IEEE), SHAHRIAR SARMAST GHAHFAROKHI[1], (Graduate Student Member, IEEE), ENES AYAZ[1], (Graduate Student Member, IEEE), MARC HILLER[2], (Senior Member, IEEE), AND HANS-PETER NEE[1], (Fellow, IEEE)

[1]School of Electrical Engineering and Computer Science, KTH Royal Institute of Technology, 11428 Stockholm, Sweden
[2]Power Electronic Systems (PES), Electrical Engineering Institute (ETI), Karlsruhe Institute of Technology (KIT), 76131 Karlsruhe, Germany

Corresponding author: Khizra Abbas (khizra@kth.se)

This work was supported by the Swedish Energy Agency under Project 44833-1.

ABSTRACT Soft-switching inverters are essential for achieving high efficiency and low electromagnetic interference (EMI) in electric vehicle (EV) drive systems. However, designing filter inductors for such converters remains challenging. In sinusoidal triangular current mode (S-TCM)-based zero-voltage-switching (ZVS) inverters, the inductor is subjected to large triangular current ripple, intentional bidirectional current operation for ZVS, and variable switching frequency, making conventional fixed-frequency PWM inductor design approaches unsuitable. This paper presents a systematic design methodology for a high-power filter inductor specifically developed for S-TCM-based ZVS inverters. The proposed methodology combines analytical design calculations, experimental characterization of the magnetic material, and finite-element-method (FEM)-based electromagnetic and loss analysis. A 3C91 ferrite pot core and three winding configurations—Litz wire, copper foil, and solid copper wire—were investigated. The inductance of the designed inductors was validated experimentally and through FEMM and ANSYS simulations, while magnetic and winding losses were evaluated using FEM-based simulations in ANSYS. The core-loss coefficients of the 3C91 ferrite material were also experimentally determined for accurate loss estimation. Two parallel inductors per phase were employed to satisfy the required inductance and current-handling capability. The proposed methodology provides a practical framework for the systematic design and evaluation of high-power filter inductors by enabling accurate prediction of inductance, magnetic losses, winding losses, and thermal performance for S-TCM-based ZVS inverters used in EV powertrains and other high-frequency power conversion systems.

INDEX TERMS Electric vehicle (EV) drive systems, filter inductor design, sinusoidal triangular current mode (S-TCM), zero-voltage switching (ZVS), finite element analysis (FEA), ferrite core characterization, winding design, core loss modeling.

I. INTRODUCTION

Electric vehicle (EV) technology is rapidly evolving to meet the growing demand for higher efficiency and higher power density [1]. These improvements directly impact overall performance, driving dynamics, and driving range, which are critical goals for the EV industry [2]. A critical component of EV powertrain systems is the traction inverter, which converts DC power from the battery into AC power for the motor. Therefore, the design and optimization of the traction inverter significantly influence the performance, efficiency, and reliability of EVs [1].

The associate editor coordinating the review of this manuscript and approving it for publication was Arman Oshnoei.

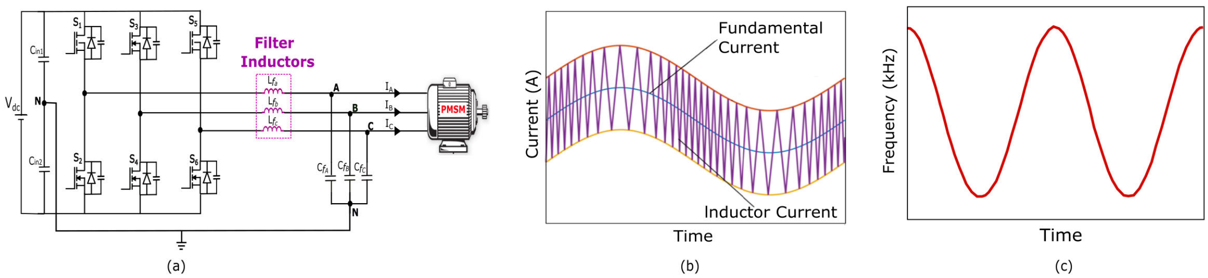

FIGURE 1. **Schematic and operational characteristics of a TCM-based ZVS inverter for an EV drive system: (a) Circuit schematic with filter inductors. (b) Variation in filter inductor current for one fundamental cycle. (c) Corresponding variable switching frequency for one fundamental cycle.**

The EV industry has traditionally relied on IGBT-based inverters using pulse-width modulation (PWM) techniques [3]. However, the emergence of wide bandgap (WBG) materials, particularly silicon carbide (SiC), has enabled improvements in inverter efficiency, power density, and switching performance due to their higher switching capability, lower switching losses, and superior thermal performance [4]. Despite these advantages, the high-speed switching characteristics of SiC devices introduce significant electromagnetic interference (EMI) challenges [5], such as high-voltage slew rates (dv/dt) and the generation of high-frequency common-mode voltages [6]. To address these issues, soft-switching techniques [7], such as zero-voltage switching (ZVS) [8], have been widely adopted. ZVS minimizes switching losses by ensuring that the voltage across the switch is approximately zero during switching transitions.

To achieve ZVS in a half-bridge configuration, triangular current mode (TCM) operation is employed, where the inductor current is intentionally driven into a bidirectional triangular waveform to provide the required commutation current for soft switching [9]. The peak value of the triangular current follows a sinusoidal envelope, enabling ZVS operation over a wide operating range. For this purpose, an LC low-pass filter is placed between the inverter output and the motor terminals, as illustrated in Fig. 1(a). While dv/dt filters are commonly adopted in many EV drive systems to limit voltage slew rates and suppress high-frequency EMI, the LC filter considered in this work is selected according to the current ripple requirements and operating characteristics of the TCM-based ZVS inverter.

In a TCM-based ZVS inverter, the filter inductor performs two primary functions. First, it enables turn-on ZVS by briefly resonating with the switch capacitance at the peak of the bidirectional current [10]. Second, it serves as an essential inductive element in the LC filter, attenuating the high-frequency current ripple through the filter capacitor to provide smooth, sinusoidal voltage and current waveforms for the motor [5], thereby enhancing power quality and minimizing EMI in the drive system.

A sinusoidal-TCM (S-TCM) modulation scheme as described in [11] is used in the ZVS inverter as illustrated in Fig. 1(b). This modulation technique bounds a sinusoidal reference current within a predefined band, ensuring that the inductor current remains within controlled limits. The S-TCM modulation method plays a critical role in shaping the inductor current waveform, thereby achieving soft switching and significantly reducing switching losses [12]. Unlike conventional fixed-frequency PWM, S-TCM employs a variable switching frequency to maintain ZVS over a wide operating range, resulting in varying switching cycles as shown in Fig. 1(c). Consequently, the inductor current consists of a low-frequency fundamental component with a large high-frequency triangular ripple component. This ripple is intentionally introduced to achieve soft-switching operation, but it also significantly affects the magnetic operating conditions of the inductor.

The unique current characteristics of S-TCM significantly influence the filter inductor design. The large bidirectional ripple current increases the peak and RMS current stresses, affecting conductor sizing, copper losses, magnetic flux density variation, and saturation limits. Furthermore, the variable switching frequency changes the magnetic excitation conditions, resulting in frequency-dependent core and winding losses. Therefore, conventional inductor design approaches developed for fixed-frequency PWM converters cannot be directly applied to S-TCM-based ZVS inverters.

The implementation of a TCM-based ZVS inverter enables highly efficient EV drive systems, with inverter efficiency reaching approximately 99.5% [2], [13]. However, enhancing inverter efficiency alone does not guarantee optimal system performance. Minimizing losses in other components, particularly the filter inductor, is crucial to achieving the desired overall efficiency [14].

The inductor losses mainly consist of core and winding losses. Core losses depend on magnetic flux density variation and excitation frequency, whereas winding losses are affected by DC resistance and high-frequency AC effects, including skin and proximity effects [15], [16]. Therefore, accurate estimation of these losses is essential for designing high-current inductors for S-TCM-based ZVS operation.

For the considered 100 kW EV traction application, the inductor experiences peak currents up to 660 A with significant current ripple. Such demanding operating conditions require careful selection of the magnetic core, air-gap length,

TABLE 1. Comparison of inductor designs based on literature.

Ref.	Inductor Design	Core Geometry & Material	Winding Configuration	Air Gap	Inductance	Freq.	Current	Power
[17]	Filter inductor for TCM-based ZVS inverter (low current)	Pot core, ferrite 3C97	Litz wire, rectangular copper	5.2 mm	5 μH	40–140 kHz	848 A (peak)	300 kW
[18]	Resonant inductor for ZVS inverter	UU79/119/31 ferrite cores	Barrel and foil windings	6 mm	10 μH	16 kHz	419.3 A (peak)	100 kW
[19]	High-frequency filter inductor	Pot core, Fair-Rite 67	Solid round copper	Dist. gaps	16.6 μH	3 MHz	2 A (peak)	250 W
[20]	Multi-frequency WPT inductor	Modified pot core, Fair-Rite 67	Solid round copper	4.2 mm	241 nH @ 13.56 MHz	MHz	3 A (peak)	70 W
[21]	AC boost inductor (3-phase PWM)	E/U cores (ferrite, amorphous, powder)	Round, Litz, foil, flat wires	Equal gaps	–	5–80 kHz	41 A (fund.)	20 kW

and winding configuration to achieve low losses while avoiding core saturation and excessive thermal stress.

A. RESEARCH GAP

Several studies have investigated high-current inductor design, focusing on magnetic-core selection, air-gap optimization, and winding technologies to reduce core and copper losses [17], [18], [19], [20], [21]. Various magnetic materials, core geometries, air-gap configurations, and winding technologies, including Litz wire, copper foil, and solid conductors, have been explored, as summarized in Table 1.

As shown in Table 1, most existing design methodologies have been developed for conventional PWM converters or soft-switching converters operating at fixed or narrow-range switching frequencies. Consequently, they do not explicitly consider the large triangular current ripple, intentional bidirectional current operation, and continuously varying switching frequency inherent to S-TCM-based ZVS inverters. Although [17] investigated a filter inductor for a TCM-based ZVS inverter, the design targeted partial-load operation with lower current requirements. Therefore, a comprehensive design methodology that simultaneously addresses high current stress, large ripple current, variable switching frequency, core selection, air-gap optimization, and winding loss evaluation for high-power S-TCM-based ZVS inverters is still lacking.

To address this gap, this paper proposes a systematic magnetic design methodology for a high-power filter inductor used in S-TCM-based ZVS inverters. The proposed methodology integrates analytical design calculations, experimental magnetic characterization, and FEM-based electromagnetic and loss analysis to optimize the core structure, air-gap length, and winding configuration under realistic EV traction inverter operating conditions.

B. RESEARCH OBJECTIVES AND CONTRIBUTIONS

This paper presents a systematic design methodology for a high-power filter inductor for S-TCM-based ZVS inverters operating with large ripple current and variable switching frequency.

The main contributions of this work are summarized as follows:

1) A magnetic design methodology is developed that incorporates the S-TCM current waveform and variable switching-frequency operation into the selection of the inductance, magnetic core, air gap, and winding configuration.
2) The effects of air-gap length and fringing flux on inductance, magnetic field distribution, and winding losses are investigated using analytical calculations, finite-element simulations, and experimental validation, providing practical guidelines for air-gap selection.
3) Litz wire, copper foil, and solid copper windings are quantitatively evaluated under identical operating conditions using finite-element simulations to compare their DC losses, AC losses, and overall suitability for high-current S-TCM-based ZVS applications.
4) A high-power filter inductor for a 100 kW EV traction inverter is designed and evaluated through finite-element simulations, demonstrating reliable operation under high-current and variable-switching-frequency conditions.

II. SYSTEM SPECIFICATIONS

Fig. 1(a) illustrates the filter inductor configuration in a capacitor-decoupled TCM-based ZVS three-phase inverter for EV drive systems. The corresponding system specifications are shown in Table 2.

TABLE 2. Specifications of EV inverter.

Symbol	Description	Value
P_r	Rated power	100 kW
V_{dc}	DC-link voltage	500 V
f_o	Fundamental frequency	50 Hz
$I_{L(1)}$	Fundamental phase current	300 A
C_f	Filter capacitance (Polypropylene)	140 μF
$----$	SiC MOSFET (C3M0016120K)	1200 V, 250 A
$R_{\mathrm{ds,on}}$	Drain-to-source on-state resistance	16 mΩ
C_{sn}	Snubber capacitance	1 nF

For S-TCM modulation, the required filter inductance is given by [11]:

$$L_{\mathrm{f}} \geq \frac{V_{\mathrm{dc}}/4}{f_{\mathrm{sw(min)}}(t)\,\Delta i_L(t)}\left[1 - M^2 \sin^2(\omega_{\mathrm{ac}} t)\right], \qquad (1)$$

where V_{dc} is the DC-link voltage, $\Delta i_L(t)$ is the peak-to-peak ripple current of inductor, $f_{\mathrm{sw(min)}}(t)$ is the minimum switching frequency, and M is the modulation index.

The minimum switching frequency is selected as 50 kHz to ensure a practical balance between switching losses and the size of the magnetic components. A lower switching frequency would increase the required inductance, leading to bulky and less efficient magnetic components. With 50 kHz, the required inductance remains feasible, and the component volume is minimized, yielding an inductance of approximately 0.72 μH.

The fundamental frequency varies from 0 to 500 Hz in the EV drive system depending on the motor operating speed. For the inductor design and loss evaluation, a representative fundamental frequency of 50 Hz is selected. Although the fundamental frequency influences the low-frequency current envelope, the dominant inductor losses are primarily caused by the high-frequency triangular current ripple and the variable switching frequency introduced by the S-TCM operation.

The filter inductor design considers two key operating scenarios: peak power (100 kW) during short-duration acceleration, where maximum currents must not saturate the core, and continuous cruising power (30 kW), which governs thermal stability. Table 3 summarizes the inductor's performance characteristics for both operational modes.

TABLE 3. Specifications of filter inductor.

Symbol	Description	Value
$f_{sw(min)}$	Minimum switching frequency	50 kHz
L_f	Filter inductance	0.72 μH
	Case 1: 100 kW Rated Power	
ΔI_L	Ripple in inductor current	660 A
$I_{L(max)}$	Maximum inductor current	630 A
$I_{L(min)}$	Minimum inductor current	-30 A
$I_{L(avg)}$	Average inductor current	300 A
$I_{L(rms)}$	RMS inductor current	285 A
	Case 1: 30 kW Rated Power	
ΔI_L	Ripple in inductor current	200 A
$I_{L(max)}$	Maximum inductor current	190 A
$I_{L(min)}$	Minimum inductor current	-10 A
$I_{L(avg)}$	Average inductor current	90 A
$I_{L(rms)}$	RMS inductor current	86 A

In the proposed system, the inductor current comprises two main components of comparable magnitude: the fundamental sinusoidal component and the high-frequency triangular component. The inductor's RMS current must account for both contributions, given by

$$I_{L,\mathrm{rms}} = \sqrt{\frac{\hat{I}_{\mathrm{sin}}^2}{2} + \frac{\hat{I}_{\mathrm{tri}}^2}{3}}, \tag{2}$$

where $\hat{I}_{\mathrm{sin}}$ is the sinusoidal output current and $\hat{I}_{\mathrm{tri}}$ is the peak of the triangular switching current.

III. INDUCTOR DESIGN CONSIDERATIONS

The proposed filter inductor design methodology is illustrated in the flowchart shown in Fig. 2. Based on the system specifications presented in Section II, the design process first establishes the magnetic requirements imposed by the S-TCM-based ZVS operation and subsequently determines the core, number of turns, air-gap length, and winding configuration.

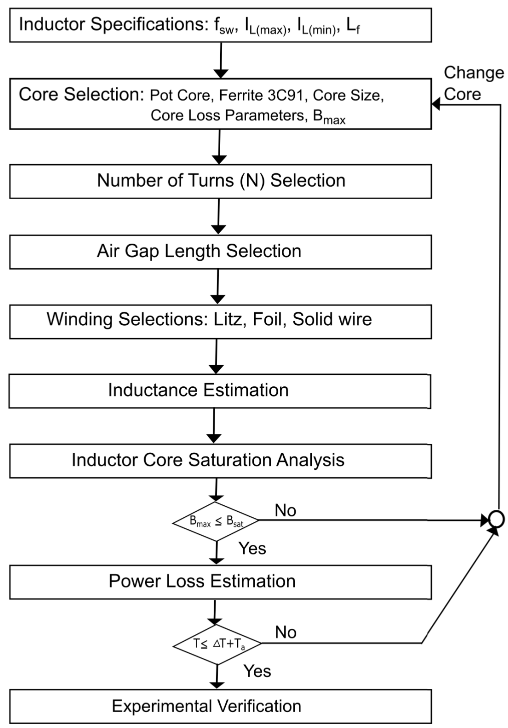

FIGURE 2. Flowchart of the filter inductor design methodology.

A. INFLUENCE OF S-TCM-BASED ZVS OPERATION ON INDUCTOR DESIGN

The operating characteristics of the S-TCM-based ZVS inverter directly determine the electrical and magnetic requirements of the filter inductor. Based on the S-TCM current ripple requirement, the minimum filter inductance is selected as 0.72 μH, as derived in Section II. Under the rated 100 kW operating condition, the inductor current varies from -30 A to 630 A, resulting in a peak-to-peak ripple current of 660 A.

These operating conditions directly define the magnetic design requirements. The magnetic core must provide sufficient cross-sectional area and withstand the required flux density variation without saturation under the maximum current variation. Therefore, the air-gap length and number of turns are determined based on the required inductance and maximum allowable flux density. Furthermore, the variable switching-frequency operation of S-TCM requires a core material with low magnetic losses over the operating frequency range, while the large high-frequency ripple current requires a winding configuration that minimizes AC losses caused by skin and proximity effects.

Accordingly, the core selection, number of turns, air-gap design, and winding configuration presented in the following subsections are derived from the operating requirements of the S-TCM-based ZVS inverter rather than conventional PWM operation. Although the presented design is developed for S-TCM operation, the same design methodology can be extended to other modulation strategies by updating the required inductance, current ripple, switching-frequency range, and soft-switching requirements according to the corresponding inductor current waveform.

B. CORE SELECTION

The selection of the magnetic core material and geometry significantly influences the performance of the filter inductor, affecting core losses, inductance, saturation behavior, thermal performance, and energy storage capability [22]. The core material determines the magnetic loss characteristics and maximum flux density, while the core geometry defines the available magnetic cross-sectional area, winding window, and magnetic field distribution.

MnZn ferrites are widely used in high-frequency power electronic applications due to their low core losses, high electrical resistivity, and good thermal stability [23]. These properties make ferrite materials suitable for high-frequency and high-power applications, such as EV traction inverter systems. However, under high-current excitation, the increased magnetizing force can drive the magnetic core toward saturation, reducing inductance and increasing losses. Therefore, an air gap is introduced to increase the magnetic reluctance, reduce the effective permeability, improve the linearity of the B–H characteristic, and enhance the energy storage capability of the inductor [24].

The core geometry also affects the magnetic field distribution and electromagnetic compatibility of the inductor. Pot-core geometries provide effective magnetic flux confinement by enclosing the winding structure, thereby reducing external leakage fields and EMI emissions [19]. This feature is particularly beneficial in EV drive systems where compact integration and electromagnetic performance are critical.

In this work, the commercially available P66/56-3C91 pot core [25] is selected because it provides sufficient magnetic cross-sectional area and winding window to accommodate the required current, energy storage capability, and winding arrangement. Furthermore, its commercial availability enables practical implementation and experimental validation of the proposed inductor design. The material properties and geometric parameters of the selected core are summarized in Table 4.

C. NUMBER OF TURNS CALCULATION

The number of turns is a key design parameter in determining the inductance and flux density within the core. In a TCM-based ZVS inverter, the inductor experiences a large current ripple, leading to a maximum flux density $B_{\max}$.

The number of turns (N) is calculated by

$$N = \frac{L \cdot I_{\mathrm{pk}}}{B_{\max} \cdot A_e}, \tag{3}$$

TABLE 4. Material and geometric specifications of the P66/56-3C91 ferrite core.

Symbol	Description	Value
	Core Material Properties	
–	Core type	Ferrite
–	Core composition	MnZn
–	Core material	3C91
–	Core geometry	Pot core
–	Core manufacturer	Ferroxcube
–	Product number	P66/56-3C91
B_{sat}	Saturation magnetic flux density	320 mT
$B_{\max}$	Maximum magnetic flux density	240 mT (75% of B_{sat})
μ_r	Relative permeability	2490
	Geometric Parameters of P66/56 Pot Core	
D_{out}	Outer diameter	66 mm
H	Core height	32 mm
l_e	Effective magnetic path length	123 mm
A_e	Effective cross-sectional area	717 mm^2
$A_{\min}$	Minimum cross-sectional area	591 mm^2
W_a	Window area	585 mm^2
m	Mass of core set	≈ 550 g

L is the inductance, I_{pk} is the peak current, A_e is the effective core cross-sectional area, and $B_{\max}$ is the maximum flux density. When L, I_{pk}, and $B_{\max}$ are fixed, N is determined by the effective core cross-sectional area A_e.

D. AIR GAP LENGTH SELECTION

A single air gap is introduced in the center of the core leg. This air gap helps regulate the inductance while ensuring that the core is not saturated.

The inductance is given by

$$L = \frac{N^2}{\mathcal{R}} = \frac{\mu_0 N^2}{\left(\dfrac{l_g}{A_{\min}} + \dfrac{l_e}{\mu_r A_e}\right)}, \tag{4}$$

where L is the inductance, N is the number of turns, $\mathcal{R}$ is the magnetic reluctance, μ_0 is the permeability of free space, l_g is the air gap length, $A_{\min}$ is the minimum core cross-sectional area, l_e is the effective magnetic path length, A_e is the effective core cross-sectional area, and μ_r is the relative permeability of the core material.

For peak-peak inductor current (660 A), the filter inductor requires an air gap length of 9.2 mm, as calculated using (4). Table 5 summarizes the key parameters for the filter inductor design.

TABLE 5. Filter inductor key parameters.

Symbol	Description	Value
L	Filter inductance	0.72 μH
N	Number of turns	3
$B_{\max}$	Magnetic flux density	240 mT
l_g	Air gap length	9.2 mm

E. WINDING SELECTION

The winding conductor must be designed to carry the rated current while maintaining acceptable copper losses and thermal performance. For the 30 kW operating condition, the calculated RMS inductor current is $I_{L(\text{rms})} = 86\,\text{A}$.

The inductor current consists of a low-frequency fundamental component superimposed with a high-frequency triangular ripple generated by the S-TCM switching operation. Therefore, the conductor is sized based on the RMS current, which determines the copper losses and thermal loading, rather than the peak current.

An RMS current density of $J_{\text{rms}} = 3.5\,\text{A/mm}^2$ is selected as the design criterion. This value provides a practical compromise between conductor cross-sectional area, copper losses, thermal performance, and winding compactness.

The required conductor cross-sectional area is calculated as,

$$A_{\text{conductor}} = \frac{I_{\text{L(rms)}}}{J_{\text{rms}}} = \frac{86}{3.5} \approx 24.6\,\text{mm}^2. \tag{5}$$

The selected conductor area is subsequently evaluated by calculating the DC and AC winding losses over the operating frequency range. Three winding configurations, namely Litz wire, copper foil, and solid round copper wire, are considered to satisfy the required conductor area while minimizing winding losses.

1) LITZ WIRE

Litz wire is widely used in high-frequency power electronic applications to reduce AC winding losses caused by skin and proximity effects [26]. It consists of multiple insulated strands twisted together to improve current distribution and reduce high-frequency losses [27]. The selection of Litz wire requires a trade-off between reduced eddy-current losses and increased DC resistance due to insulation and reduced copper fill factor. Therefore, the strand diameter and number of strands are selected to minimize the total winding loss.

The skin depth is calculated as

$$\delta = \sqrt{\frac{\rho}{\pi f \mu_0}},$$

where ρ is the conductor resistivity and μ_0 is the permeability of free space.

Considering the high-frequency S-TCM operation, the calculated skin depth is approximately 0.1 mm. Therefore, the maximum allowable strand cross-sectional area is

$$A_{\text{strand}} = \pi\delta^2 = \pi(0.1)^2 = 0.0314\ \text{mm}^2.$$

Based on the required conductor cross-sectional area of $24.6\,\text{mm}^2$, the required number of strands is

$$N_{\text{strand}} = \frac{A_{\text{conductor}}}{A_{\text{strand}}} = \frac{24.6}{0.0314} \approx 784.$$

Therefore, a commercially available Litz wire consisting of 800 strands, each with a radius of 0.1 mm [28], is selected. The selected Litz wire satisfies the required conductor area and fits within the available winding window. The parameters of the selected Litz wire are summarized in Table 6.

2) COPPER FOIL

Copper foil is widely used in high-current inductors due to its large conductor surface area, which reduces DC resistance and improves heat dissipation [29]. However, the foil thickness must be carefully selected to reduce AC losses caused by skin and proximity effects [30].

For the proposed inductor, a copper foil thickness of 0.2 mm [31] is selected considering AC loss performance, mechanical handling, and commercial availability. The selected thickness is comparable to the skin-depth requirement under the high-frequency excitation introduced by the S-TCM operation, thereby limiting additional eddy-current losses. The available winding window limits the foil width to 38 mm, and a practical width of 36 mm is selected. The cross-sectional area of one foil is

$$A_{\text{foil}} = 0.2 \times 36 = 7.2\ \text{mm}^2.$$

The required number of parallel foils is calculated as

$$N_{\text{foil}} = \frac{24.6}{7.2} = 3.42.$$

Therefore, four parallel copper foils are selected to satisfy the required conductor area while fitting within the available winding window. The specifications of the selected copper foil are summarized in Table 6.

3) SOLID ROUND COPPER WIRE

Solid round copper wire is an attractive winding option because of its low cost, simple fabrication, and wide commercial availability. However, at high switching frequencies, its AC resistance increases due to skin and proximity effects, which must be considered during conductor selection [32].

For the proposed inductor, the solid conductor size is selected based on the required copper cross-sectional area of $24.6\,\text{mm}^2$ while maintaining compatibility with the available core window. Multiple parallel solid conductors are used to achieve the required current-carrying capability and to reduce the impact of high-frequency AC resistance. The selected conductor arrangement provides a practical compromise between copper utilization, manufacturability, and winding losses. The specifications of the selected solid copper conductors are summarized in Table 6.

IV. RESULTS AND DISCUSSIONS

This section presents the results of the inductor design, including inductance estimation, factors influencing inductance, core saturation analysis, power loss analysis, and power dissipation of inductors.

A. INDUCTANCE ESTIMATION AND MEASUREMENT

Inductance estimation was performed using both FEMM and ANSYS Maxwell to enable cross-validation and improve confidence in the results. Introducing an air gap in the ferrite pot core highlights the effect of fringing flux, which significantly influences the total inductance and is not captured in analytical models that ignore fringing.

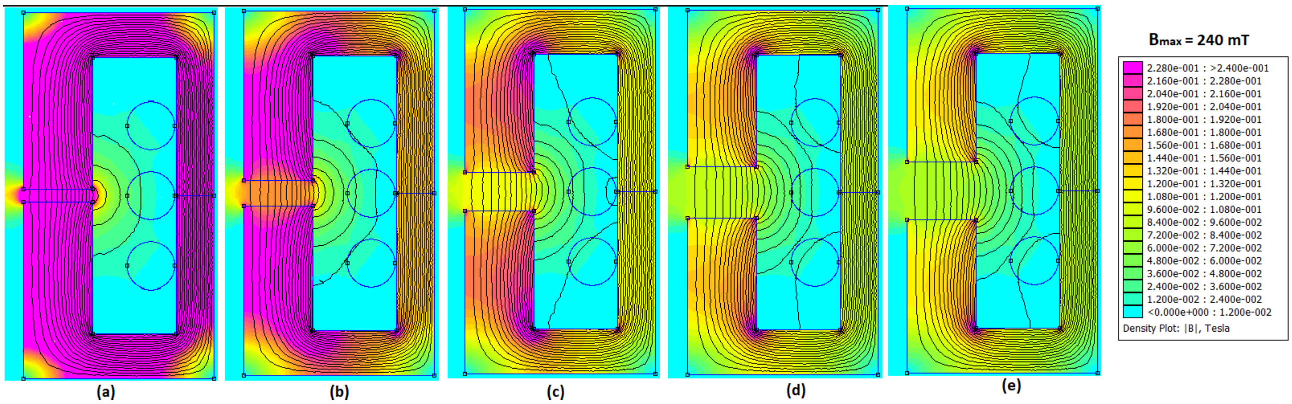

FIGURE 3. Impact of air gap length on the fringing field and inductance using FEMM simulation for a 30 kW power Litz-based inductor. (a) Air gap length = 2 mm. (b) Air gap length = 4 mm. (c) Air gap length = 6 mm. (d) Air gap length = 8 mm. (e) Air gap length = 9.2 mm.

TABLE 6. Winding specifications.

Parameter	Value
Litz Wire Parameters	
Single strand radius	0.1 mm
Single strand cross-sectional area	0.0314 mm^2
Number of strands	800
Litz wire cross-sectional area	25.12 mm^2
Litz wire diameter	7.5 mm
Litz wire coating	(2 × Nylon) Serving
Copper Foil Parameters	
Foil thickness	0.2 mm
Foil width	36 mm
Single foil cross-sectional area	7.2 mm^2
Number of parallel foils	4
Number of layers	3
Solid Round Copper Wire Parameters	
AWG number	14
Bare wire diameter	1.63 mm
Bare wire cross-sectional area	2.082 mm^2
Number of parallel wires	12
Number of turns	3

1) IMPACT OF AIR GAP LENGTH ON FRINGING FLUX

Fringing flux occurs around the air gap as magnetic flux lines spread outward while passing through the non-magnetic gap. This increases the magnetic field's cross-sectional area, reducing flux density, known as the fringing field effect [33].

The influence of air-gap length on the fringing flux distribution was investigated using FEMM simulations with Litz-wire windings while maintaining a constant operating frequency and current, as illustrated in Fig. 3. The air-gap length was varied from 2 mm to 9.2 mm.

The simulation results show that increasing the air-gap length causes the magnetic flux to spread progressively into the surrounding air. For small air gaps, the fringing field remains localized near the center leg of the pot core, as shown in Fig. 3(a) and Fig. 3(b). As the air-gap length increases further, the fringing field extends significantly beyond the center leg and into the surrounding region, as illustrated in Fig. 3(c)–(e).

Increasing the air-gap length increases the magnetic reluctance, which reduces the overall inductance. However, the resulting fringing field enlarges the effective magnetic cross-sectional area around the air gap, leading to inductance values that are higher than those predicted by analytical models that neglect fringing effects. At the same time, the extended fringing field penetrates the nearby windings, increasing eddy-current losses and the AC winding resistance.

To minimize these additional winding losses, the conductors are positioned away from the air-gap region, thereby reducing their exposure to the fringing field. Therefore, the air-gap length must be carefully selected to achieve an appropriate balance among energy-storage capability, core saturation margin, inductance accuracy, and winding losses.

2) FRINGING FIELD EFFECT IN DIFFERENT INDUCTORS

Fig. 4 shows the fringing field effect in three different inductors, simulated using FEMM. In the Litz wire inductor, the flux is concentrated near the air gap length, with a small amount of fringing flux extending into the outer leg of the pot core. In the foil winding inductor, the fringing flux is concentrated on the top layer of the foil, close to the air gap. In the solid copper wire inductor, the fringing flux extends all over to the outer leg of the pot core. These variations affect AC resistance and winding losses differently in each design.

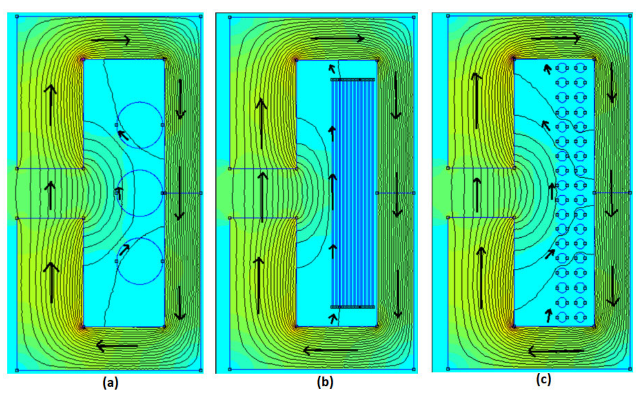

FIGURE 4. Fringing field effect in different inductors using FEMM simulation at 8 mm air gap length. (a) Litz-inductor. (b) Foil-inductor. (c) Solid wire-inductor.

3) EXPERIMENTAL DESIGN OF DIFFERENT INDUCTORS

To validate the analytical and simulation results, prototypes of the three proposed inductor configurations were fabricated using Litz wire, copper foil, and solid round copper wire, as shown in Fig. 5. The inductance of each prototype was measured using a Bode 100 impedance analyzer, as illustrated in Fig. 6.

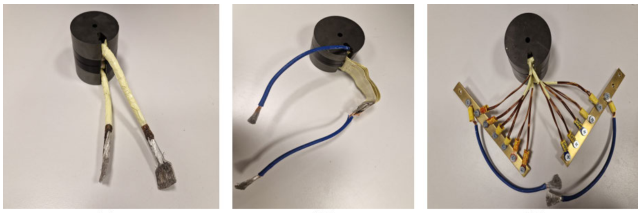

(a) (b) (c)

FIGURE 5. Experimental prototypes of the designed inductors. (a) Litz wire inductor. (b) Copper foil inductor. (c) Solid round copper wire inductor.

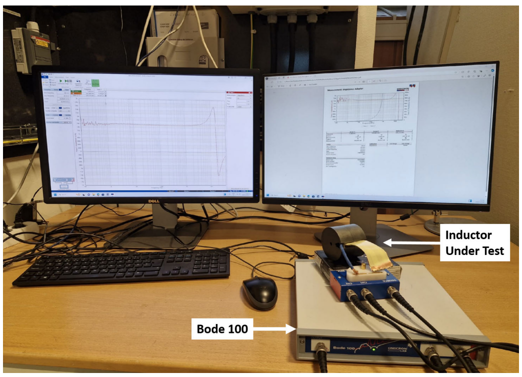

FIGURE 6. Inductance estimation using Bode 100.

4) IMPACT OF AIR GAP LENGTH ON INDUCTANCE

The inverse relationship between inductance and air gap length is demonstrated in Fig. 7.

As the air gap increases, inductance decreases due to the reduced total permeance. The analytical model, which neglects the fringing field effect, predicts lower inductance values compared to FEMM simulations, which account for fringing flux and show higher inductance. This deviation grows with larger air gaps, emphasizing the importance of considering fringing flux in practical designs. Experimental results align closely with FEMM simulations, confirming the model's accuracy and highlighting the limitations of the analytical approach.

5) SELECTION OF 8 MM AIR GAP OVER 9.2 MM

An ideal analytical model, which neglects the fringing-field effect, suggested a 9.2 mm air gap to achieve an inductance of 0.72 μH. However, FEMM simulations revealed that the fringing field becomes significantly more pronounced at this air-gap length. Therefore, an 8 mm air gap was selected because it better confines the magnetic field around

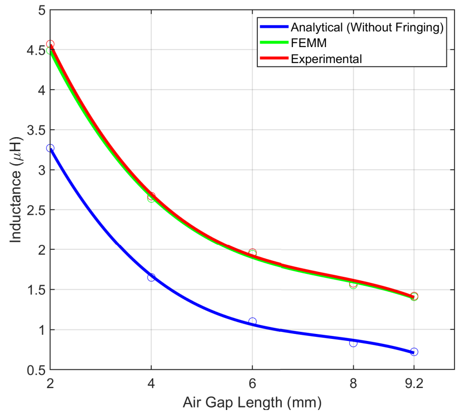

FIGURE 7. Inductance variation with air-gap length for the ferrite pot-core inductor: analytical calculation without fringing effects, FEMM simulation including fringing effects, and experimental measurement using Litz-wire winding.

the air-gap region, reducing the exposure of the winding to the fringing field. Based on the observed fringing-field distribution, this is expected to reduce the additional AC winding losses associated with fringing flux while maintaining the required inductance.

6) COMPARISON OF INDUCTANCE MEASUREMENTS AT 8 MM AIR GAP

Table 7 compares inductance values obtained through analytical calculations (ignoring fringing), FEMM simulations, ANSYS Maxwell, and experimental measurements. The analytical model significantly underestimates inductance due to disregarding the fringing effects. FEMM and ANSYS simulations closely match experimental results, confirming their reliability. Litz wire and solid wire inductors show better alignment between FEMM and experimental data, while the copper foil shows a minor discrepancy with ANSYS.

TABLE 7. Inductance estimation at 8 mm air gap by analytical, simulated, and experimental methods.

Inductor	Analytical	FEMM	ANSYS	Experimental
Litz wire	0.83 μH	1.55 μH	1.54 μH	1.58 μH
Copper foil	0.83 μH	1.47 μH	1.37 μH	1.48 μH
Solid wire	0.83 μH	1.55 μH	1.47 μH	1.51 μH

7) OPTIMIZATION OF INDUCTOR GEOMETRY TO ACHIEVE TARGET INDUCTANCE

An 8 mm air gap results in nearly twice the required inductance. To achieve the target of 0.72 μH, two configurations were evaluated: (1) two parallel inductors with three turns each, and (2) a single inductor with two turns. Table 8 summarizes the inductance and average switching frequency with varying switching cycles for both setups at 100 kW.

Although both configurations provide inductance values slightly higher than the analytical target, the difference has limited impact on the current ripple because the S-TCM

TABLE 8. Inductor inductance and switching frequency at maximum power.

Configuration	Power	Inductance	Avg. Switching Frequency
Parallel (3 turns)	100 kW	0.77 μH	147 kHz
Single (2 turns)	100 kW	0.833 μH	136 kHz

current reference is controlled by the inverter operation. However, the increased inductance affects the switching-frequency range, which may influence the output voltage ripple and the associated magnetic and semiconductor losses. Therefore, the final configuration is selected considering the trade-off between inductance accuracy, winding losses, thermal performance, and practical implementation.

B. CORE SATURATION RISK ASSESSMENT FOR HIGH-POWER OPERATION

At 100 kW, analytical calculations using (3) indicate peak flux densities of 220 mT for the 3-turn parallel inductor and 331 mT for the 2-turn single inductor. The 3C91 datasheet [25] specifies a saturation threshold of 320 mT at 100°C and 25 kHz. As shown in Fig. 8, the 3-turn parallel configuration exhibits a more uniform flux distribution with reduced fringing, whereas the 2-turn design shows higher flux concentration and pronounced fringing, increasing the risk of localized saturation.

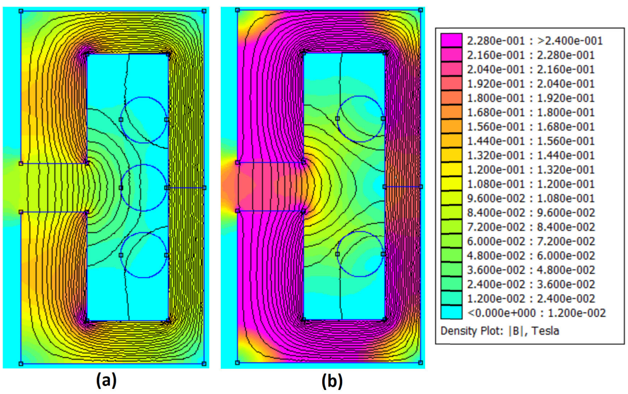

FIGURE 8. Magnetic flux density and fringing field in different inductor configurations using FEMM simulation. (a) 3-turn parallel inductor. (b) 2-turn single inductor.

The 2-turn inductor also conducts the full current through a single winding, leading to higher copper losses and elevated winding and core temperatures. Combined with increased flux and frequency, this raises core losses and thermal stress.

Thus, the 2-turn inductor is less suitable for high-power operation due to:

- Excessive magnetic flux density, exceeding the core's saturation limit,
- Higher fringing fields leading to local hot spots and possible localized saturation,
- Increased copper losses due to full current conduction through a single winding,
- Greater core losses from elevated flux and frequency, risking thermal runaway.

The 3-turn parallel configuration is preferred, as it mitigates core saturation risk, reduces thermal stress, and ensures reliable high-power operation.

C. INDUCTOR POWER LOSS ANALYSIS

To accurately evaluate the core and winding losses of the proposed parallel inductor design across different winding configurations in a P66/56 core, the 3C91 ferrite loss coefficients are first determined experimentally. These coefficients are subsequently used in finite-element simulations to predict losses under realistic operating conditions.

1) EXPERIMENTAL DETERMINATION OF 3C91 CORE LOSS PARAMETERS

The core loss parameters K, α, and β, known as Steinmetz parameters, are experimentally determined by measuring the core losses of 3C91 magnetic material across a range of excitation frequencies and peak magnetic flux densities (100 mT to 250 mT). These parameters are derived using the Steinmetz equation:

$$P_c = Kf^{\alpha}B^{\beta}, \tag{6}$$

where P_c is the core-loss density (W/m^3), f is the excitation frequency (Hz), B is the peak magnetic flux density (T), and K, α, and β are material-dependent Steinmetz coefficients.

The experimental setup, as illustrated in Figure 9, comprises several key components. The Core Under Test (CUT) is a pot core made of 3C91 material from Ferroxcube. It is wound with 3 turns of 1.6 mm diameter solid copper wire for AC excitation. A resonance circuit is utilized to drive the CUT. Different capacitors are used to achieve resonance at the selected test frequencies. A signal generator produces a sinusoidal voltage waveform, while a power amplifier drives the CUT at sufficient excitation levels without core saturation. An isolation transformer is used to prevent ground loops during measurements, with a digital oscilloscope monitoring waveforms.

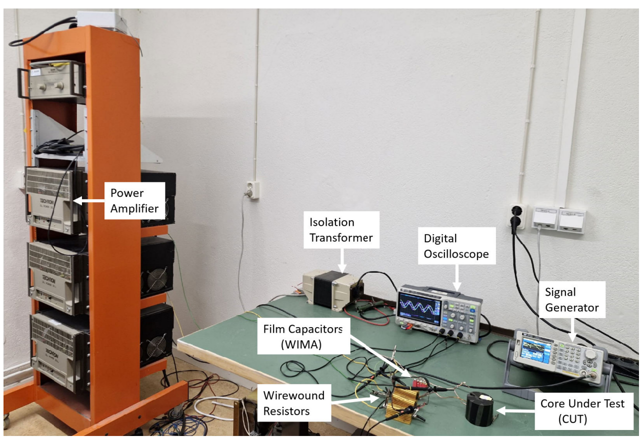

FIGURE 9. Experimental setup for core characterization.

The measurement system includes a digital oscilloscope to monitor voltage and current waveforms. Data acquisition is conducted via USB, capturing input voltage, inductor voltage, and resistor voltage to facilitate core loss calculations.

The circuit current is measured using three parallel-connected ARCOL NHS series non-inductive aluminium-housed wire-wound resistors [34] placed in series with the CUT winding, while high-frequency passive voltage probes are used to measure the voltage at critical circuit nodes.

A sinusoidal excitation signal is applied to the CUT at three distinct frequencies (50 kHz, 100 kHz, and 140 kHz). The excitation voltage is adjusted to avoid core saturation while ensuring sinusoidal voltage and current waveforms. The peak magnetic flux density B is derived from the induced voltage in the CUT windings using the relationship:

$$B = \frac{2V_L}{NA_e 2\pi f},$$

where V_L is the induced voltage, N is the number of turns, A_e is the effective core cross-sectional area, and f is the excitation frequency. Fig. 10 shows the measured voltage and current waveforms at 50 kHz.

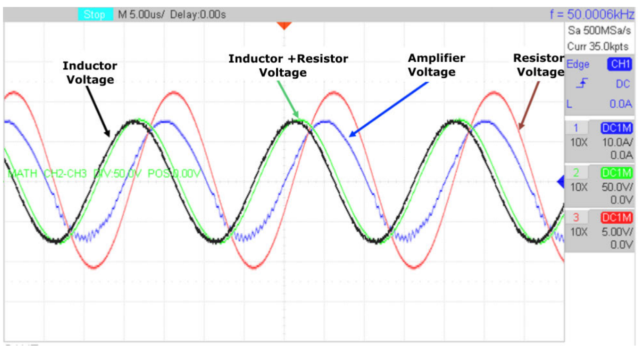

FIGURE 10. Measured voltage and current waveforms at 50 kHz.

The total input power is calculated as

$$P_{\text{total}} = V_{\text{rms}} I_{\text{rms}} \cos\phi,$$

where V_{rms} and I_{rms} are the measured RMS voltage and current, respectively, and ϕ is the phase angle between them.

The copper loss was calculated using the experimentally measured AC winding resistance. The winding resistance was measured using an LCR meter at the corresponding excitation frequency, including the frequency-dependent effects of skin and proximity losses.

$$P_{\text{copper}} = I_{\text{rms}}^2 R_{\text{AC}},$$

where I_{rms} is the measured RMS winding current and R_{AC} is the measured AC winding resistance.

The core loss is then extracted by subtracting the copper loss contribution from the total input power:

$$P_{\text{core}} = P_{\text{total}} - P_{\text{copper}}.$$

The measured core loss density was obtained over a range of excitation frequencies and magnetic flux densities to characterize the magnetic loss behavior of the 3C91 ferrite material. The measured data were then used to extract the Steinmetz parameters through linear regression applied to the logarithmic form of (6). The resulting core loss characteristics are presented in Fig. 11 and Fig. 12.

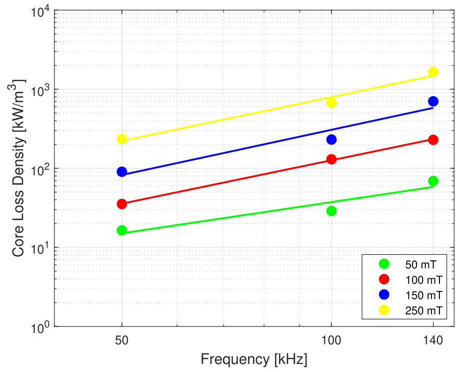

FIGURE 11. Power loss density of 3C91 ferrite at 25°C and 0 mT DC bias as a function of excitation frequency.

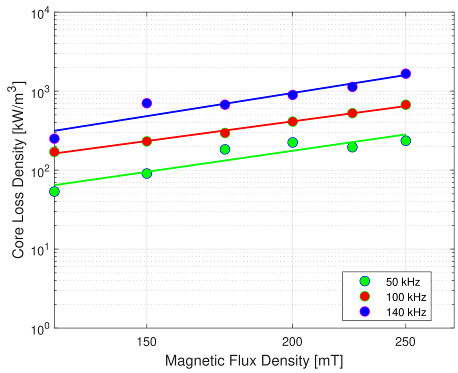

FIGURE 12. Power loss density of 3C91 ferrite at 25°C and 0 mT DC bias as a function of peak magnetic flux density.

2) FINITE-ELEMENT LOSS ANALYSIS AND VALIDATION

The experimentally extracted Steinmetz parameters are incorporated into ANSYS Maxwell to evaluate the core and winding losses of the proposed inductor design. Initially, a 2D eddy current analysis is performed to estimate the inductance under AC excitation. However, the steady-state assumption of this approach limits its capability to accurately capture the time-varying loss behavior because the inductor operates with a continuously varying current waveform due to the 50 Hz fundamental component and the high-frequency S-TCM ripple current.

To overcome this limitation, transient simulations are performed to evaluate the instantaneous core and winding losses. An autonomous gate driver (AGD) [35] model is implemented in ANSYS Twin Builder, as shown in Fig. 13, to generate realistic S-TCM inductor current waveforms.

The transient simulations capture the dynamic loss behavior during switching transitions, where rapid variations in the magnetic flux produce instantaneous increases in both core

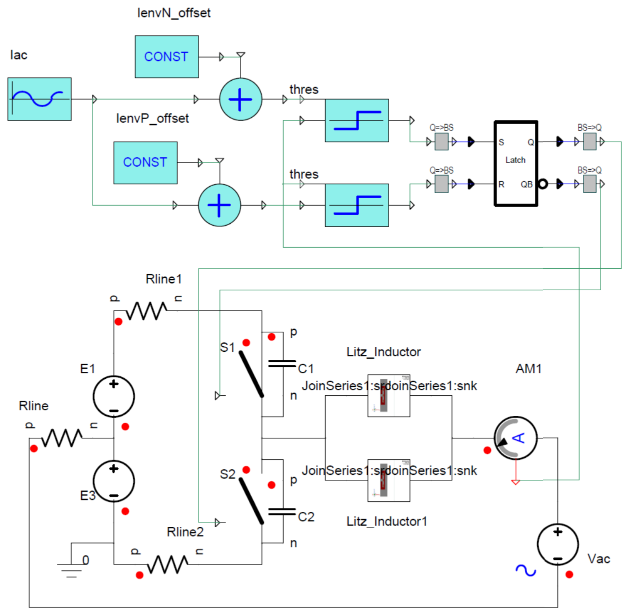

FIGURE 13. Autonomous gate drivers (AGDs) in ANSYS Twin Builder.

and winding losses. Fig. 14 presents the instantaneous core and winding losses for the 3-turn inductor at 30 kW under low- and high-average-current operating conditions.

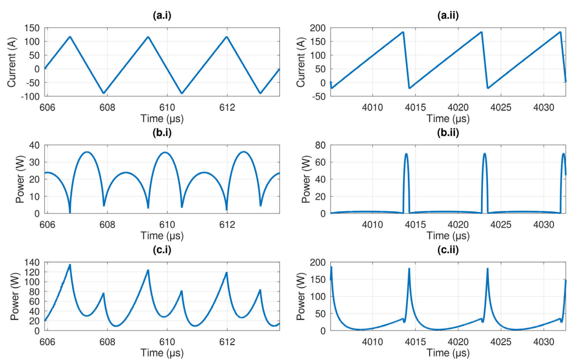

FIGURE 14. Transient losses in the 3-turn inductor at 30 kW under (i) low-average-current and (ii) high-average-current operating conditions: (a.i) filter current, (b.i) core losses, (c.i) winding losses; (a.ii) filter current, (b.ii) core losses, and (c.ii) winding losses.

The results in Fig. 14 show transient spikes in both core and winding losses during switching events. The increase in core loss is mainly associated with the rapid variation of magnetic flux during switching transitions, which increases the hysteresis and eddy-current losses in the ferrite core.

Although the switching frequency is maximum near the current zero-crossing, the instantaneous winding loss remains relatively low because the RMS current is small. In contrast, near the peak current region, the switching frequency decreases, but the substantially larger current magnitude increases the RMS current and therefore the copper loss according to the I^2R relationship. Consequently, the simulated winding loss increases from approximately 20 W near the zero-crossing to approximately 180 W near the peak current. These results indicate that, for the proposed S-TCM operation, the winding loss is dominated by the RMS current, while the switching frequency mainly influences the AC resistance through skin and proximity effects.

3) COMPARISON OF WINDING CONFIGURATIONS

Table 9 presents a comparison of Litz wire, copper foil, and solid wire windings under 30 kW and 100 kW operating conditions. Litz wire consistently exhibits the lowest total losses due to reduced AC winding losses, achieving 15 W at 30 kW and 85 W at 100 kW. In contrast, solid wire results in significantly higher losses, particularly at high frequencies, reaching 48 W and 196 W, respectively.

These results demonstrate the superior efficiency of Litz wire for high-frequency applications, making it the preferred choice for the proposed inductor design.

TABLE 9. Operational parameters and losses.

Inductor Type	Litz Wire	Copper Foil	Solid Wire
Case 1: 30 kW Rated Power			
Peak-Peak Inductor Current Envelope (A)	200	200	200
Inductance (μH)	0.76	0.65	0.77
Avg Switching Freq. (kHz)	441	498	459
Core Losses (W)	5	4	6
Winding Losses (W)	10	20	42
Total Losses per Inductor (W)	15	24	48
Total Losses for Six Inductors (W)	**90**	**144**	**288**
Case 2: 100 kW Rated Power			
Peak-Peak Inductor Current Envelope (A)	660	660	660
Inductance (μH)	0.77	0.67	0.73
Avg Switching Freq. (kHz)	147	166	153
Core Losses (W)	21	13	15
Winding Losses (W)	64	79	181
Total Losses per Inductor (W)	85	92	196
Total Losses for Six Inductors (W)	**510**	**552**	**1176**

D. THERMAL MANAGEMENT AND POWER DISSIPATION OF INDUCTORS

The maximum power loss at 60°C, according to the pot core datasheet [25], is 52 W. In contrast, the proposed inductor design results in a maximum power loss of 15 W, indicating adequate thermal management. To maintain the winding temperature within safe limits, Litz wire winding can be used with plastic insulation, offering good thermal conductivity for efficient heat transfer.

To further enhance heat dissipation, the inductor is mounted directly on the EV chassis, which serves as a heat sink, lowering thermal resistance. Additionally, metallic heat-spreading plates or dedicated heat sinks are employed to improve cooling. Thermal interface materials (TIMs), such as thermal grease or pads, are applied to optimize heat transfer between the inductor and chassis, ensuring effective heat dissipation and safe operating temperatures.

V. CONCLUSION

This paper presented a systematic design methodology for high-power filter inductors used in S-TCM-based ZVS inverters with variable switching frequency. The proposed approach considers the unique operating characteristics of S-TCM, including large current ripple, switching-frequency variation, and soft-switching requirements. Three winding configurations (Litz wire, copper foil, and solid copper wire) using 3C91 ferrite pot cores with an 8 mm air gap were investigated. The required inductance of 0.72 μH was achieved through a parallel inductor configuration.

The key findings of this study are summarized as follows:

- An inductor design comprising six inductors (two parallel inductors per phase), each measuring 57 mm $\times$ 66 mm, was developed to satisfy the required inductance and current-handling capability.
- The influence of air-gap length and fringing flux was experimentally and numerically analyzed, demonstrating the importance of considering fringing effects for accurate inductance prediction and winding loss estimation.
- Experimental characterization of the 3C91 ferrite core enabled the extraction of frequency-dependent core loss parameters, which were used for accurate magnetic loss evaluation.
- Among the investigated winding configurations, the Litz wire winding provided the best performance by reducing AC winding losses and limiting temperature rise under high-frequency ripple excitation.
- The thermal performance of the proposed inductor can be improved by mounting the magnetic components on the EV chassis, which acts as an additional heat sink and reduces thermal resistance.
- The designed Litz-wound inductor maintained stable magnetic performance at the 100 kW operating condition and acceptable thermal performance at 30 kW operation, confirming its suitability for high-power EV traction applications.

The results demonstrate that high-power inductors for S-TCM-based ZVS inverters require simultaneous consideration of inductance accuracy, fringing-field effects, winding AC losses, and thermal management. The proposed design methodology provides a practical framework for designing efficient magnetic components for S-TCM-based ZVS inverter applications.

ACKNOWLEDGMENT

The authors acknowledge the use of ChatGPT (OpenAI) for limited language editing to improve the clarity and grammar of the manuscript. The tool was not used to generate the scientific content, experimental results, analysis, interpretations, or conclusion.

REFERENCES

[1] M. S. Khan, S. S. Nag, A. Das, and C. Yoon, "Analysis and control of an input-parallel output-series connected buck-boost DC–DC converter for electric vehicle powertrains," *IEEE Trans. Transport. Electrific.*, vol. 9, no. 2, pp. 2015–2025, Jun. 2023.

[2] M. Jahnes, L. Zhou, Y. Fahmy, and M. Preindl, "A peak 1.2-MHz, >99.5% efficient, and >10-kW/L power dense soft-switched inverter for EV fast charging applications," *IEEE Trans. Transport. Electrific.*, vol. 10, no. 3, pp. 5520–5532, Sep. 2024.

[3] J. Reimers, L. Dorn-Gomba, C. Mak, and A. Emadi, "Automotive traction inverters: Current status and future trends," *IEEE Trans. Veh. Technol.*, vol. 68, no. 4, pp. 3337–3350, Apr. 2019.

[4] Y. Yan, C. Chen, Z. Wu, J. Guan, J. Lv, and Y. Kang, "A high power density double-side-end double-sided bonding SiC half-bridge power module," *IEEE Trans. Transport. Electrific.*, vol. 9, no. 2, pp. 3149–3163, Jun. 2023.

[5] M. Haider, P. S. Niklaus, M. Madlener, G. Rohner, and J. W. Kolar, "Comparative evaluation of gate driver and LC-filter based dv/dt-limitation for SiC-based motor-integrated variable speed drive inverters," *IEEE Open J. Power Electron.*, vol. 4, pp. 450–462, 2023.

[6] Q. Li, X. Zhang, Z. Zhang, Q. Luo, Y. Ma, and C. Yuan, "An optimized zero-CM PWM for symmetry and suppression of circulating current in paralleled inverters applied to AC motor drives," *IEEE Trans. Transport. Electrific.*, vol. 11, no. 1, pp. 682–692, Feb. 2025.

[7] D. Xu, R. Li, N. He, J. Deng, and Y. Wu, *Soft-Switching Technology for Three-Phase Power Electronics Converters*. Hoboken, NJ, USA: Wiley, 2021.

[8] C. P. Henze, H. C. Martin, and D. W. Parsley, "Zero-voltage switching in high frequency power converters using pulse width modulation," in *Proc. APEC 88 3rd Annu. IEEE Appl. Power Electron. Conf. Expo.*, New Orleans, LA, USA, Nov. 1988, pp. 33–40, doi: 10.1109/APEC.1988.10548.

[9] C. Marxgut, J. Biela, and J. W. Kolar, "Interleaved triangular current mode (TCM) resonant transition, single phase PFC rectifier with high efficiency and high power density," in *Proc. Int. Power Electron. Conf. - ECCE ASIA*, Jun. 2010, pp. 1725–1732.

[10] S. Miric, P. S. Niklaus, J. Huber, C. Stäger, M. Haider, and J. W. Kolar, "Analysis and experimental verification of the EMI signature of three-phase three-level TCM soft-switching converter systems," *IEEE Access*, vol. 11, pp. 57391–57400, 2023.

[11] M. Haider, J. A. Anderson, S. Miric, N. Nain, G. Zulauf, J. W. Kolar, D. Xu, and G. Deboy, "Novel ZVS S-TCM modulation of three-phase AC/DC converters," *IEEE Open J. Power Electron.*, vol. 1, pp. 529–543, 2020.

[12] M. Haider, J. A. Anderson, N. Nain, G. Zulauf, J. W. Kolar, D. Xu, and G. Deboy, "Analytical calculation of the residual ZVS losses of TCM-operated single-phase PFC rectifiers," *IEEE Open J. Power Electron.*, vol. 2, pp. 250–264, 2021.

[13] K. Abbas and H.-P. Nee, "Autonomous gate drivers tailored for triangular current mode-based zero-voltage switching two-level three-phase inverters for electric vehicle drive systems," *Energies*, vol. 17, no. 5, p. 1060, Feb. 2024.

[14] Y.-Y. Huang and Y.-S. Lai, "Optimal inductor design method for GaN-based PFC," *IEEE Access*, vol. 11, pp. 104452–104462, 2023, doi: 10.1109/ACCESS.2023.3317332.

[15] P. L. Dowell, "Effects of eddy currents in transformer windings," *Proc. Inst. Electr. Engineers*, vol. 113, no. 8, pp. 1387–1394, 1966, doi: 10.1049/piee.1966.0236.

[16] R. P. Wojda and M. K. Kazimierczuk, "Magnetic field distribution and analytical optimization of foil windings conducting sinusoidal current," *IEEE Magn. Lett.*, vol. 4, 2013, Art. no. 0500204, doi: 10.1109/LMAG.2013.2255864.

[17] B. Chatterjee, J. Allgeier, T. Plum, and M. Hiller, "A partial load three-phase triangular current mode modulation concept with an optimized filter inductor for high efficiency traction drives," in *Proc. PCIM Eur.*, 2024, pp. 774–783.

[18] C. Du, W. G. Hurley, and D. Xu, "Design methodology of resonant inductor in a ZVS inverter," *IEEE J. Emerg. Sel. Topics Power Electron.*, vol. 3, no. 4, pp. 1142–1150, Dec. 2015.

[19] R. S. Yang, A. J. Hanson, B. A. Reese, C. R. Sullivan, and D. J. Perreault, "A low-loss inductor structure and design guidelines for high-frequency applications," *IEEE Trans. Power Electron.*, vol. 34, no. 10, pp. 9993–10005, Oct. 2019.

[20] R. S. Yang, I. Nikiforidis, N. Pucci, M. V. Joisher, P. Wagle, P. D. Mitcheson, and D. J. Perreault, "Design and performance comparison of multi-frequency inductors for megahertz wireless power transfer," in *Proc. IEEE Appl. Power Electron. Conf. Expo. (APEC)*, Long Beach, CA, USA, Feb. 2024, pp. 861–868.

[21] R. M. Burkart, H. Uemura, and J. W. Kolar, "Optimal inductor design for 3-phase voltage-source PWM converters considering different magnetic materials and a wide switching frequency range," in *Proc. Int. Power Electron. Conf. (IPEC-Hiroshima - ECCE ASIA)*, Hiroshima, Japan, May 2014, pp. 891–898.

[22] M. R. Kiran, M. R. Islam, K. M. Muttaqi, D. Sutanto, and R. Raad, "A comprehensive review of advanced core materials-based high-frequency magnetic links used in emerging power converter applications," *IEEE Access*, vol. 12, pp. 107769–107799, 2024, doi: 10.1109/ACCESS.2024.3436562.
[23] M. Kacki, M. S. Rylko, J. G. Hayes, and C. R. Sullivan, "Measurement methods for high-frequency characterizations of permeability, permittivity, and core loss of Mn-Zn ferrite cores," *IEEE Trans. Power Electron.*, vol. 37, no. 12, pp. 15152–15162, Dec. 2022, doi: 10.1109/TPEL.2022.3189671.
[24] R. Jez, "Influence of the distributed air gap on the parameters of an industrial inductor," *IEEE Trans. Magn.*, vol. 53, no. 11, pp. 1–5, Nov. 2017, doi: 10.1109/TMAG.2017.2699120.
[25] Ferroxcube. *P66/56 Pot Core*. Accessed: Aug. 2024. [Online]. Available: https://www.ferroxcube.com/upload/media/product/file/Pr_ds/P66_56.pdf
[26] C. R. Sullivan and R. Y. Zhang, "Simplified design method for litz wire," in *Proc. IEEE Appl. Power Electron. Conf. Expo. - APEC*, Fort Worth, TX, USA, Mar. 2014, pp. 2667–2674, doi: 10.1109/APEC.2014.6803681.
[27] C. R. Sullivan, "Optimal choice for number of strands in a Litz-wire transformer winding," *IEEE Trans. Power Electron.*, vol. 14, no. 2, pp. 283–291, Mar. 1999, doi: 10.1109/63.750181.
[28] Pack Litz Wire. *Litz Wires Products*. Accessed: Jun. 30, 2026. [Online]. Available: https://www.packlitzwire.com/products/litz-wires/
[29] A. H. Ismail, Z. Ma, A. Al-Hmoud, and Y. Zhao, "A high frequency coupled inductor design for high power density DC–DC converters," in *Proc. IEEE Appl. Power Electron. Conf. Expo. (APEC)*, Orlando, FL, USA, Mar. 2023, pp. 3275–3280, doi: 10.1109/APEC43580.2023.10131629.
[30] A. Khan, D. Waheed, M. B. Siddiqui, M. S. Anwer, S. W. Hussain, and I. A. Makda, "Design and comparative analysis of Litz and copper foil transformers for high frequency applications," in *Proc. 20th Eur. Conf. Power Electron. Appl. (EPE ECCE Europe)*, Sep. 2018, pp. 1–10.
[31] *Copper Foil Product Page*. Accessed: Oct. 2024. [Online]. Available: https://www.svb24.se/sv/kopparfolie-0-2-x-60-mm.html
[32] R. P. Wojda and M. K. Kazimierczuk, "Analytical optimization of solid–round-wire windings," *IEEE Trans. Ind. Electron.*, vol. 60, no. 3, pp. 1033–1041, Mar. 2013, doi: 10.1109/TIE.2012.2189543.
[33] M. K. Kazimierczuk and H. Sekiya, "Design of AC resonant inductors using area product method," in *Proc. IEEE Energy Convers. Congr. Expo.*, San Jose, CA, USA, Sep. 2009, pp. 994–1001.
[34] ARCOL. *NHS Series Non-Inductive Aluminium Housed Wirewound Resistors*. Accessed: Oct. 2024. [Online]. Available: https://www.arcolresistors.com/products/nhs-series/
[35] K. Abbas, L. P. Gandla, S. S. Ghahfarokhi, K. Kostov, and H.-P. Nee, "Autonomous gate drivers for TCM-based soft-switched converters: Design approach and experimental validation," *IEEE Trans. Ind. Electron.*, vol. 73, no. 6, pp. 8354–8365, Jun. 2026, doi: 10.1109/TIE.2026.3654760.

KHIZRA ABBAS (Member, IEEE) received the M.Phil. degree in physics from Government College University, Lahore, Pakistan, in 2012, the M.S. degree in system dynamics from the University of Bergen, Bergen, Norway, in 2016, and the Ph.D. degree in electrical engineering from KTH Royal Institute of Technology, Stockholm, Sweden, in 2025.

She was a Teaching Assistant with KTH Royal Institute of Technology, from 2019 to 2025, where she contributed to power electronics education and research activities within EU-funded projects. Her research interests include high-power magnetic component design, soft-switching power converters, autonomous gate drivers, and high-efficiency electric vehicle traction inverters. Her work focuses on the design, analysis, and experimental validation of advanced power electronic systems with emphasis on improving efficiency, power density, and reliability.

BHASKAR CHATTERJEE (Student Member, IEEE) received the M.Sc. degree in electrical power engineering from RWTH Aachen University, Aachen, Germany, in 2015. He is currently pursuing the Ph.D. degree with the Institute of Electrical Engineering, Karlsruhe Institute of Technology (KIT), Karlsruhe, Germany, and a Power Electronics Developer at Robert Bosch GmbH, Germany. His research interests include power electronics, electric vehicle drive systems, high-efficiency inverter topologies, triangular current mode (TCM) modulation, zero-voltage-switching (ZVS) converters, and magnetic component design. His research focuses on the analysis and optimization of high-frequency power electronic converters, including magnetic loss evaluation, switching loss reduction, and advanced modulation techniques for electric vehicle applications. He received the Best Paper Award at the PCIM Europe 2024 for his work on the partial-load TCM inverter.

ANTONIO CAMEO DEL REY (Student Member, IEEE) received the M.Sc. degree in electrical engineering from KTH Royal Institute of Technology, Stockholm, Sweden, in 2025. His research interests include power electronic converters, electric vehicle drive systems, soft-switching techniques, zero-voltage-switching (ZVS) converters, and electromagnetic compatibility (EMC) in high-voltage power electronics. His work focuses on the analysis, design, and testing of high-efficiency power conversion systems.

SHAHRIAR SARMAST GHAHFAROKHI (Graduate Student Member, IEEE) was born in Isfahan, Iran, in 1994. He received the B.Sc. and M.Sc. degrees in electronics engineering and power electronics engineering from Sharif University of Technology, Tehran, Iran, in 2018 and 2020, respectively. He is currently pursuing the Ph.D. degree with KTH Royal Institute of Technology, Stockholm, Sweden. His research interests include power electronics, electric vehicles, wireless power transfer, and renewable energy systems.

ENES AYAZ (Graduate Student Member, IEEE) received the B.Sc. and M.Sc. degrees in electrical and electronics engineering from Middle East Technical University (METU), Ankara, Türkiye, in 2019 and 2022, respectively, with a focus on power electronics. He is currently pursuing the Ph.D. degree in power electronics with KTH Royal Institute of Technology, Stockholm, Sweden. His research interests include high-voltage SiC-based traction inverters for heavy-duty electric vehicles, including inverter topology optimization, advanced PWM modulation techniques, and system-level loss and efficiency optimization.

MARC HILLER (Senior Member, IEEE) received the Diploma degree in electrical engineering from the Technische Universität Darmstadt, Darmstadt, Germany, in 1993, and the Ph.D. degree in electrical engineering from the Universität der Bundeswehr München, Neubiberg, Germany, in 2008. From 2005 to 2015, he was with Siemens Industry, Nuremberg, Germany, as a Project Manager and the Head of Power Section Development with the Research and Development Department for low-and medium-voltage converters for energy and industrial applications. He is currently with Karlsruhe Institute of Technology (KIT), Karlsruhe, Germany, as a Full Professor for power electronic systems and the Head of the Institute of Electrical Engineering (ETI). His current research interests include the areas of design and control of advanced high-power electronics systems and high-performance drives.

HANS-PETER NEE (Fellow, IEEE) was born in Västerås, Sweden, in 1963. He received the M.Sc., Licentiate, and Ph.D. degrees in electrical engineering from KTH Royal Institute of Technology, Stockholm, Sweden, in 1987, 1992, and 1996, respectively. Since 1999, he has been a Professor in power electronics with the Department of Electrical Engineering, KTH Royal Institute of Technology. His research interests include power electronic converters, semiconductor components, and the control aspects of power electronic systems for transportation, utility applications, high-voltage direct-current transmission, and variable-speed drives.